J. Fluid Mech. (2021), *vol*. 911, A43, doi:10.1017/jfm.2020.1052

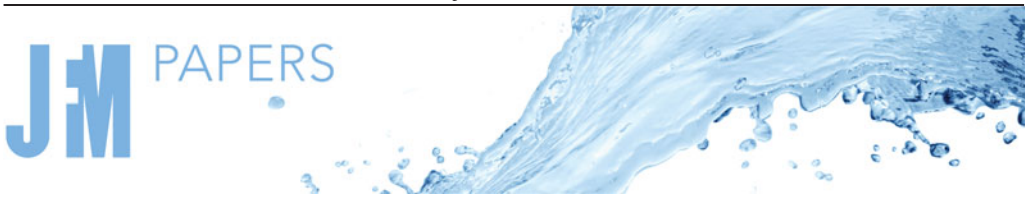

Stepwise transitions in spin-up of rotating Rayleigh–Bénard convection

D. Noto[1],†, Y. Tasaka[1], T. Yanagisawa[1,2] and T. Miyagoshi[2]

[1]Laboratory for Flow Control, Faculty of Engineering, Hokkaido University, Sapporo 060-8628, Japan

[2]Japan Agency for Marine-Earth Science and Technology (JAMSTEC), Yokosuka, Kanagawa 237-0061, Japan

(Received 27 April 2020; revised 8 September 2020; accepted 18 November 2020)

Transient behaviours during spin-up in rotating Rayleigh–Bénard convection (RBC) with imposed rotation were quantitatively investigated in laboratory experiments. Horizontal and vertical velocity fields were measured by particle image velocimetry with water as the test fluid. Varying the aspect ratio, Rayleigh number and Taylor number, a total of twenty parameters were systematically explored. Toroidal and spiral rolls were formed when the flow reached the rigid-body rotation state, and creation of these structures propagated from the rim towards the internal regions together with the development of the spin-up. Alternate alignments of rolls with opposite meridional circulation transported azimuthal momentum in the rigid-body rotation, and a meandering velocity profile in the radial direction, induced Kelvin–Helmholtz (KH) instability generating azimuthally aligned vortices. The vortices progressively decreased in horizontal dimensions with the wall-to-centre propagation of the vortex formation, but the vortical structures remain larger than the columnar vortices formed in the equilibrium state of a rotating RBC. At the intermediate radius of the fluid layer, the wall-to-centre propagation of the roll formation was overtaken by that of the KH vortex formation. Farther into the interior region, thermal plumes forming columnar vortices were generated as separations of the thermal boundary layers, and the system reached an equilibrium state of rotating RBC dominated by columnar vortices. Use of a fluid vessel with a moderate aspect ratio clarified these transitions to occur in a stepwise fashion, and a spin-up time scale unique in the rotating RBC was found to be from a few to 10 times the Ekman time scale.

Key words: Bénard convection, rotating flows, vortex dynamics

1. Introduction

Thermal convection occurring between two horizontal plates with a vertical temperature gradient, i.e. Rayleigh–Bénard convection (RBC), is a fundamental system arising in fluid

† Email address for correspondence: noto@ring-me.eng.hokudai.ac.jp

mechanics involving large-scale fluid motion. The RBC system imposed a background rotation, the so-called rotating RBC, which has attracted much interest and has been applied to geophysical or astrophysical fluid flows (e.g. Jones 2011; Grannan *et al.* 2016). Flow morphologies observed in rotating RBC with respect to the heat transfer (the Nusselt number) variations have been detailed elsewhere, and a rotating RBC can be described by dimensionless parameters as follows. The Prandtl number defined as the ratio of the kinematic viscosity ν and the thermal diffusivity κ as

$$Pr = \frac{\nu}{\kappa}, \tag{1.1}$$

reflects the relation of the thickness of the viscous and thermal boundary layers. The Rayleigh number denotes the thermal buoyancy effect against restrictions of fluids due to the viscous and thermal diffusions as

$$Ra = \frac{g\beta\Delta T H^3}{\kappa\nu}, \tag{1.2}$$

where g, β, ΔT and H denote the gravitational acceleration, the thermal expansion coefficient, the temperature difference between top and bottom of the fluid layer, and the height of the fluid layer, respectively. The influence of the background rotation is found to be dictated by the Taylor number, defined as the ratio of the Coriolis force to the viscous force and expressed by

$$Ta = \left(\frac{2\Omega H^2}{\nu}\right)^2, \tag{1.3}$$

where Ω is the rotational speed of the background rotation. Expressed differently, the rotational effect is often expressed by the Ekman number in the form $Ek = \nu/(\Omega H^2) = 2Ta^{-1/2}$. To include both thermal and rotational forces, the convective Rossby number

$$Ro = \frac{1}{2\Omega}\sqrt{\frac{g\beta\Delta T}{H}} = \sqrt{\frac{Ra}{Pr\,Ta}}, \tag{1.4}$$

is frequently used in addition to the above. With decreasing Ro values, the flow structures in an equilibrium state of a rotating RBC with $Pr > 0.2$ may be categorized into four regimes: three-dimensional turbulence; vortical plume; convective Taylor column (CTC); and cellular regimes (Liu & Ecke 2009; Weiss & Ahlers 2011; Julien *et al.* 2012; Stevens, Clercx & Lohse 2013). Recent experimental work to elucidate the regime transitions is summarized in Cheng *et al.* (2018). In the vortical plume and the CTC regimes, columnar vortices, originating from thermal plumes stretched along a vertical (rotational) axis, dominate the flow fields. Interest in the heat transfer characteristics and flow morphologies have so far been investigated in equilibrium states of rotating RBC, i.e. fully developed states of both rotation and thermal convection. As established in Noto *et al.* (2019) the equilibrium state of a rotating RBC dominated by columnar vortices is described for various time scales, even with steady rotation.

In many actual phenomena, system rotation is not precisely steady but accompanies fluctuations, and transient behaviours associated with changes in the rotation speed may radicalize (dull) a part of the multiple time scale phenomena described above. As a typical example of transient phenomena on rotating flows, a problem of spin-up induced by a rapid change in the rotation speed has long research history and rich knowledge. With respect to rotating convection, however, detailed investigations on transient states during spin-up from an RBC at rest towards a fully developed rotating RBC are fewer and not frequently

discussed except in some experimental work (e.g. Boubnov & Golitsyn 1986; Vorobieff & Ecke 1998; Zhong, Patterson & Wettlaufer 2010) and a numerical work (Ravichandran & Wettlaufer 2020). It is worth investigating the transient behaviours observed during the spin-up process from a non-rotating RBC to a rotating RBC as a part of the multiple time scale phenomenon in rotating RBC. The earlier work imposed a rotation to a fully developed thermal convection (Boubnov & Golitsyn 1986; Vorobieff & Ecke 1998) or evaporative fluids at a rest (Zhong *et al.* 2010; Ravichandran & Wettlaufer 2020). This procedure is equivalent to providing a thermal convection as an initial state for the classical problem of a spin-up of fluid from rest as summarized in Greenspan (1968), as well as imposing thermal boundary conditions at the top and bottom flat boundaries. The previous works have reported similar transient behaviours during the spin-up of thermal convection, even when the geometries and boundary conditions of each are not identical; after imposing rotation, ring-shaped convection rolls are formed and a shear-induced Kelvin–Helmholtz (KH) instability breaks up the rolls to vortices. These transient states evolve to the equilibrium states of rotating convection which are dominated by a number of columnar vortices after a sufficiently long time. Apart from the limited investigations of spin-up of thermal convection, there is a large literature on spin-up of rotating fluids (e.g. Wedemeyer 1964; Greenspan 1968; Benton & Clark 1974; Weidman 1976). Considering the spin-up of convection, this problem can be regarded as an important phenomenon as a sort of classical spin-up problem with a special boundary condition.

The objective of this study is to provide a comprehensive explanation for the transient behaviours reported in previous works (Boubnov & Golitsyn 1986; Vorobieff & Ecke 1998; Zhong *et al.* 2010; Ravichandran & Wettlaufer 2020), associating with both the rotating convection and the classical rotating fluid dynamics. To investigate the transient behaviours during spin-up of rotating RBC systematically, we focused on imposing a rotation instantaneously to a fully developed RBC as following the former work. The parameter ranges for the vortical plumes or the CTC regime as equilibrium states are examined, $Ra = 2.0 \times 10^6$ or 1.0×10^7 and $3.0 \times 10^6 \leq Ta \leq 2.0 \times 10^8$ corresponding to $0.0378 \leq Ro \leq 0.690$. For each condition, we examined the velocity and temperature fields in the horizontal and vertical cross-sections in fluid layers of two different aspect ratios. First, we investigated the mechanism of formation of toroidal convection rolls initially appearing during the spin-up in thermal convection as described earlier. Second, the mechanism of formation of vortex structures originating in convection rolls are quantified. To sum up all of the measured results, a comprehensive explanation for the transient behaviours, and the essential spin-up time scale unique in rotating RBC, will be provided.

2. Overview of laboratory experiments

2.1. *Experimental set-up*

The experimental facilities used in the present study are detailed elsewhere (Noto *et al.* 2018, 2019) and are shown in the schematic diagrams in figure 1. A rectangular vessel composed of 15 mm-thick acrylic walls with inner geometries of $200 \times 200 \times 40$ mm^3 was used. Cylindrical fluid layers of the height of the vessel, $H = 40$ mm, were formed by placing one of two different inner radius cylinders, $R = 40$ and 95 mm, in the rectangular vessel. The resulting aspect ratios of the cylindrical fluid layers are $\Gamma = 2R/H = 2.00$ and 4.75. The bottom of the fluid layer was confined and heated by a 10 mm-thick copper plate heater, and the top of the fluid was confined and cooled by a transparent cooling device. This cooling device has an internal refrigerant chamber letting cooled water from

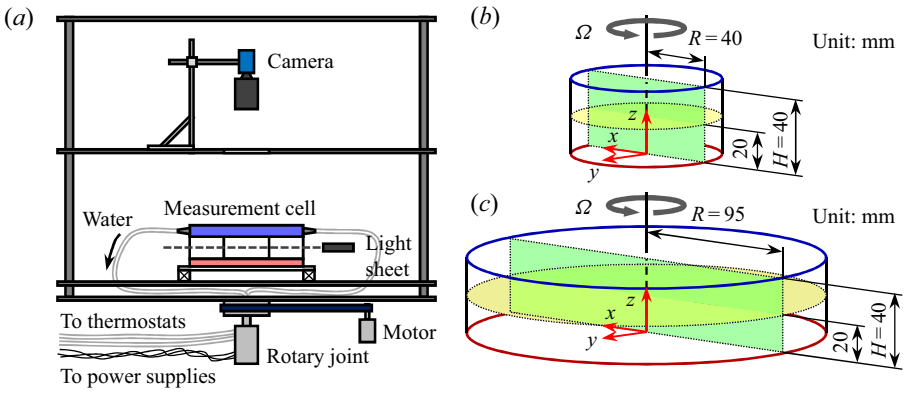

Figure 1. (*a*) Side and oblique views of the turntable, schematically illustrated, together with the measurement cell and optical devices for the horizontal cross-section visualization and geometries of two different radii cylindrical fluid layers: (*b*) $\Gamma = 2.00$ and (*c*) $\Gamma = 4.75$. Visualized cross-sections in a horizontal and a vertical plane are coloured yellow and green, respectively. Grey arrows indicate the direction of rotation.

a thermostat circulate inside the device, cooling the fluid layer through a 3 mm-thick glass plate. With this, optical visualization from the top of the fluid layer is possible through the transparent cooling device. The top and bottom temperatures were maintained constant, and monitored with thermistors throughout a single experimental run. The convective fluid motion realized in the present arrangement was described and explicated in Noto *et al.* (2018, 2019). Degassed distilled water ($Pr \sim 7$ at 20 °C) was used as the test fluid and in the cylindrical fluid layers. The gap between the rectangle walls and the cylinders were also filled with the test fluid to act as a water jacket, as well as to reduce unwanted optical distortion.

We conducted two independent series of visualization experiments by altering the optical equipment; horizontal cross-section ($z = 0.5H$) and vertical cross-section ($y = 0$) as illustrated in figure 1(*b*,*c*). For the horizontal cross-section visualization, a tiny amount of thermochromic liquid crystal (TLC) particles (mean diameter $d_p = 15$ μm, mean density $\rho_p = 1.02 \times 10^3$ kg m^3, approximate dynamic range 20–25 °C, Japan Capsular Products Inc.) were suspended in the test fluid. As shown in figure 1(*a*), a white light sheet (∼5 mm-thick) generated by a cylindrical lens and a halogen lamp illuminated the half-height ($z = 0.5H = 20$ mm) of the fluid layer. A CMOS colour camera (DFK33UP5000, The Imaging Source Co.) was mounted above the fluid layer perpendicular to the light sheet for continuous optical observations. To conduct the particle image velocimetry (PIV) analysis, the images were acquired at 25 or 40 frames per second (f.p.s.) to suit the frame rate for the PIV. For the vertical cross-section visualization, porous resin particles (mean diameter $d_p = 120$ μm, mean density $\rho_p = 1.02 \times 10^3$ kg m^3, CHP20P, Mitsubishi Chemical Co.) were suspended. A 2 W green laser sheet (<3 mm-thick) illuminated the vertical cross-section from above at the middle position ($y = 0$) coinciding with the rotational axis. Image acquisition at 25 or 40 f.p.s. was conducted by the same camera as above, set at the side of the fluid layer to be perpendicular to the laser sheet.

As shown in figure 1(*a*), all the equipment was mounted and fixed on a turntable which can rotate at the constant rotational speed of $\Omega = 0.0$–5.0 rad s^{-1} and the corresponding *Ta* is 0.0–2.8×10^8, for the present conditions. Here the rotational axis coincides with the

centre of the cylindrical fluid layers and the optical axis of the camera rotating together with the turntable, the resulting visualization images were recorded in the rotating frame.

2.2. *Experimental procedures and conditions*

To investigate the temporal evolution of the transient behaviours during the spin-up for the RBC in a rest state towards a rotating RBC, fully developed states of non-rotating RBC were realized first. The non-rotating RBC was maintained for more than 30 minutes with one temperature difference between the top and bottom boundaries. A rotation was imposed to this fully developed RBC, and the image acquisition was initiated at this time. Here the time constant of the rotational acceleration of the turntable was 1 s at any rotational speed Ω, and thus it is possible to consider that the rotation was provided as in a step function.

The experimental parameters explored in the present study are detailed in table 1. For each of the two cylinders, two different Ra values were examined at five different Ta values, and 20 parameters were explored in total. Since the horizontal and the vertical cross-section visualizations could not be conducted simultaneously, two independent experiments were conducted for each parameter, giving a total of 40 experimental runs. In a non-rotating field at the explored Ra values, $Ra = 2.0 \times 10^6$ and 1.0×10^7, the flow fields are expected to be dominated by thermally coherent structures such as thermal plumes or large-scale structures. If a sufficiently long period elapses after providing a rotation of $3.0 \times 10^6 \leq Ta \leq 2.0 \times 10^8$, the flow regimes in the present conditions lie in the vortical plume or the CTC regimes (Noto *et al.* 2018, 2019). That is, the flow structures dominated by a number of columnar vortices are expected at an equilibrium state of the rotating RBC. In addition to the principal parameters of the rotating RBC, Pr, Ra and Ta, the influence of the centrifugal force is often considered. Here, defined as the ratio of the centrifugal force to gravity,

$$Fr = \frac{R\Omega^2}{g}, \tag{2.1}$$

the Froude number is conventionally used. Also, the spin-up of a fluid at rest is characterized by the Ekman time scale τ_E (Greenspan & Howard 1963), which is defined as

$$\tau_E = \frac{H}{\sqrt{\nu\Omega}} = Ek^{1/2}\tau_\nu, \tag{2.2}$$

where $\tau_\nu = H^2/\nu$ expresses the viscous diffusion time scale. As may be considered from this formula, rigid-body rotation can be achieved at $O(10^1$ s), which is much faster than would be expected from the viscous diffusion time scale of $O(10^3$ s). Considering the rotation time scale of the system as $\tau_\Omega = 1/(2\Omega) = O(10^{-1}$ s), these three time scales are related as $\tau_\Omega \ll \tau_E \ll \tau_\nu$ (Weidman 1976). To characterize the time scale of these phenomena, the time t elapsed from imposing the rotation is normalized by the widely used Ekman time scale τ_E, and will be expressed as t^* $(= t/\tau_E)$ below.

2.3. *Qualitative observation of transient behaviours*

To understand the transition of fluid motion from a non-rotating RBC to a rotating RBC, first, visualization results from the TLC particle experiments for the horizontal cross-section will be discussed qualitatively in this § 2.3 before introducing quantitative considerations. As mentioned above, a rotation is induced in a fully developed thermally

Pr	Γ	Ra	Ta	Ro	Fr	τ_E (s)
∼7 (at 20 °C)	2.00	2.0×10^6	3.0×10^6	0.308	0.0012	54.3
			1.0×10^7	0.169	0.00402	40.1
			3.0×10^7	0.0975	0.01205	30.4
			1.0×10^8	0.0534	0.04015	22.5
			2.0×10^8	0.0378	0.0803	18.9
		1.0×10^7	3.0×10^6	0.690	0.0012	54.3
			1.0×10^7	0.378	0.00402	40.1
			3.0×10^7	0.218	0.01205	30.4
			1.0×10^8	0.119	0.04015	22.5
			2.0×10^8	0.0845	0.0803	18.9
	4.75	2.0×10^6	3.0×10^6	0.308	0.00286	54.3
			1.0×10^7	0.169	0.00954	40.1
			3.0×10^7	0.0975	0.02861	30.4
			1.0×10^8	0.0534	0.09536	22.5
			2.0×10^8	0.0378	0.19072	18.9
		1.0×10^7	3.0×10^6	0.690	0.00286	54.3
			1.0×10^7	0.378	0.00954	40.1
			3.0×10^7	0.218	0.02861	30.4
			1.0×10^8	0.119	0.09536	22.5
			2.0×10^8	0.0845	0.19072	18.9

Table 1. Experimental parameters explored in the present study. For each parameter, both the horizontal and the vertical cross-section visualization were conducted independently, resulting in 40 experimental runs being conducted.

turbulent state ($Ra > 1.0 \times 10^6$) at rest. Typical snapshots of non-rotating RBC states with different Ra values in the smaller cylinder ($\Gamma = 2.00$) are shown in figure 2. In figure 2, TLC particles provide colours corresponding to the temperature, red, green and blue as temperature increases, with the smaller Ra condition (figure 2*a*) showing relatively larger coherent structures than those for the larger Ra case (figure 2*b*). As well as the size of the thermally coherent structures, a widely distributed green colour can be seen at the smaller Ra value because the temperature difference is smaller than that with the larger Ra value (figure 2*b*). For both cases, flow structures are governed by a number of thermal plumes which are visible as red and blue spots in both panels of figure 2, the realized flow structures can be regarded as fully developed thermal turbulent structures. The temporal evolution of the spin-up state after the rotation starts in the case of $Ra = 2.0 \times 10^6$ and $Ta = 3.0 \times 10^7$ with $\Gamma = 2.00$ is shown in figure 3. Time elapses from the upper left to the lower right. Soon after imposing the rotation in the flow structures of a non-rotating RBC as in figure 2 at $t^* = 0.0$, thermally coherent structures such as thermal plumes and large-scale structures disappear and the fluid layer is nearly fully mixed. This would occur as an intense shear is suddenly induced at the vicinity of both the top and the bottom walls as well as at the sidewall. In addition, the centrifugal force drives cold (hot) fluid radially outward (inward) due to the mixed density differences in the fluid layer. Accordingly, in figure 3, the thermal plumes present in the non-rotating state swirl from the centre to the wall, and as a result a coherent colour pattern extends into the azimuthal direction and can be seen as alternative red and blue lines ($t^* = 0.2$–0.5). After the fluid is completely mixed, there is an almost uniform colouration at $t^* = 1.0$, with narrow red and blue rings appearing only at the vicinity of the sidewall. These rings eventually grow wider and the ring formation progresses from the sidewall towards the centre of the fluid layer.

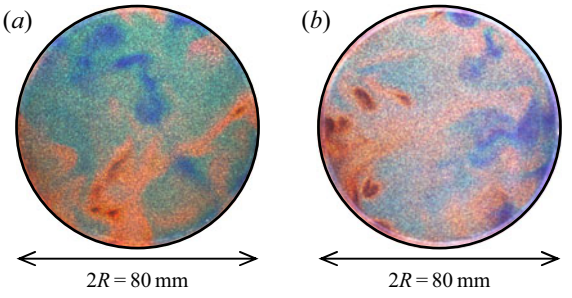

Figure 2. Snapshots of horizontal cross-sections at half-height ($z = 0.5H$) of non-rotating thermal convection in the smaller cylinder $\Gamma = 2.00$ visualized by the TLC particles: (*a*) $Ra = 2.0 \times 10^6$ and (*b*) $Ra = 1.0 \times 10^7$. Red and blue show cold and hot regions qualitatively because of the TLC colouration characteristics.

At $t^* = 2.0$ such the rings are more clearly visible than at $t^* = 1.0$. From the colouration sequence of the rings, red, blue and red again from the wall towards the centre of the fluid layer, it may be assumed that the corresponding temperatures are cold, hot and cold again as visualized by the TLC particles. Considering these colourations as temperature distributions, these rings may be regarded as horizontal slices of toroidal convection rolls; respectively, down-welling, up-welling, down-welling flows progressing from the wall to the centre. The emergence of such rolls has previously been reported by other researchers (Boubnov & Golitsyn 1986; Vorobieff & Ecke 1998; Zhong *et al.* 2010; Ravichandran & Wettlaufer 2020).

After the emergence of the concentric convection rolls, the rings start to fluctuate and meander in the azimuthal direction displaying wavy patterns at $t^* = 2.2$ of figure 3. Similar to the ring formations, this fluctuation was reported by Boubnov & Golitsyn (1986), Vorobieff & Ecke (1998) and Zhong *et al.* (2010). The fluctuations gradually increase in amplitude in the radial directions and finally form azimuthal vortex trails such as at $t^* = 2.4$ of figure 3, where there are clearly separated red (cold), blue (hot) and red (cold) vortices aligned inwards from the wall toward the centre. Expressed differently, the vortical structures form along the boundaries of the radially aligned concentric convection rolls. With time, the vortical structures grow and the formation of these progressively develop towards the centre at $t^* = 3.0$ of figure 3. However, it remains possible to distinguish the regularly aligned red and blue circles in places. The circles can be considered as the down-welling and up-welling vortices, and they are moving very slowly throughout the fluid layer as addressed by Noto *et al.* (2019). At $t^* = 4.0$ of figure 3, the fluid layers are fully governed by the vortical structures which are randomly distributed throughout the fluid layer. The final states look quite similar to the equilibrium state of a fully developed rotating RBC. Another example with $Ra = 2.0 \times 10^6$ and $Ta = 3.0 \times 10^7$ with $\Gamma = 4.75$ is shown in figure 4. Here, the radius of the large fluid layer is more than double that of the small one, even though the image sizes in figures 3 and 4 are identical. Thermally coherent structures disintegrate, and concentric convection rolls gradually form from the sidewall at $t^* = 0.2$–2.0. The number of rolls is larger than that in figure 3. The convection rolls subsequently fluctuate and form azimuthally aligned vortical structures at $t^* = 2.4$–3.0 even in the large radius fluid layer. This vortex formation progresses from the sidewall towards the centre of the fluid layer, and the final state at $t^* = 6.0$ also looks similar to the equilibrium state of a fully developed rotating RBC. While some differences can be seen between figures 3 and 4, the displayed cases show basically similar transitions from non-rotating to rotating RBC.

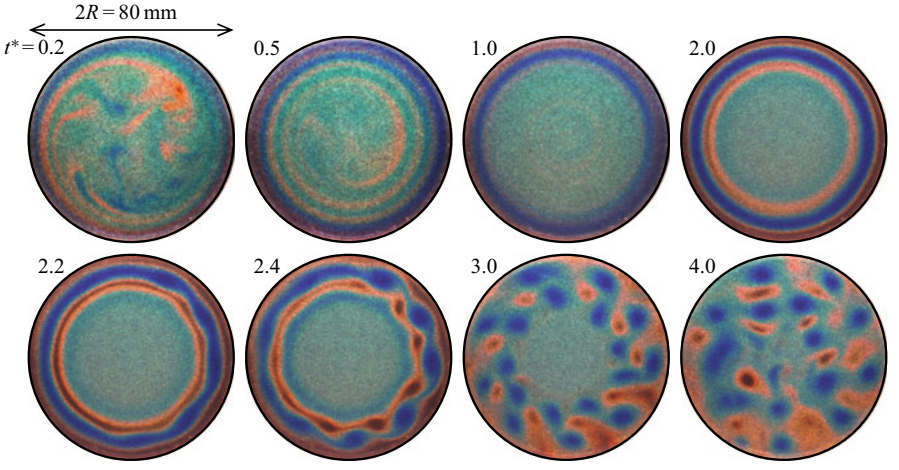

Figure 3. Temporal evolution of spin-up state after the initiation of the rotation with the condition of $Ra = 2.0 \times 10^6$ and $Ta = 3.0 \times 10^7$ in the $\Gamma = 2.00$ cylinder. Each snapshot is a horizontal cross-section at $z = 0.5H$ visualized by the TLC particles. Time elapses from top left to bottom right, and the corresponding t^* values are at the upper left of each snapshot. Please note that time intervals between the snapshots are not the same. The corresponding movie is available from the supplementary movie 1 available at https://doi.org/10.1017/jfm.2020.1052.

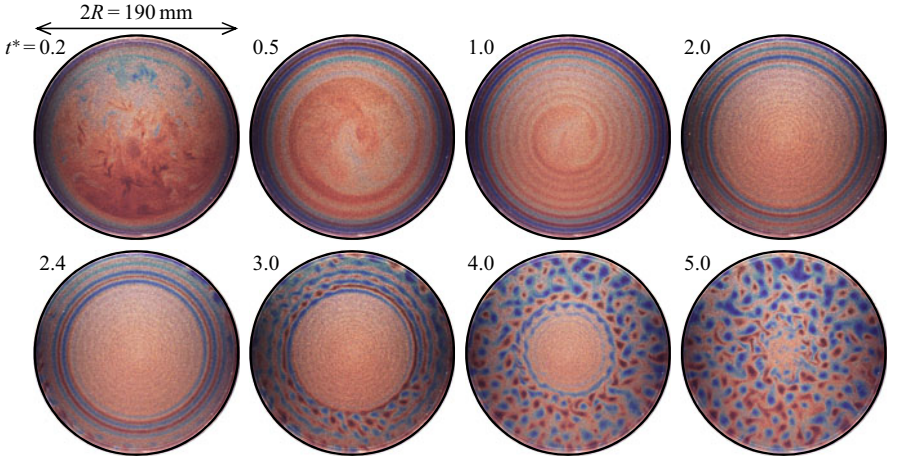

Figure 4. Temporal evolution of the spin-up state after the initiation of the rotation with the condition of $Ra = 2.0 \times 10^6$ and $Ta = 3.0 \times 10^7$ in the $\Gamma = 4.75$ cylinder. Each snapshot is a horizontal cross-section at $z = 0.5H$ visualized by the TLC particles. Time elapses from upper left to lower right, and the corresponding t^* values are noted at top left of each snapshot. Please note that time intervals between the snapshots are not constant. The corresponding movie is available from the supplementary movie 2.

Transient behaviours, which have been mentioned in Boubnov & Golitsyn (1986), Vorobieff & Ecke (1998) and Zhong *et al.* (2010), were successfully observed in the present study. First the structures of the non-rotating RBC disintegrated, and subsequently toroidal convection rolls form rings at the vicinity of the sidewall. The rings start to fluctuate in the azimuthal direction and develop into vortical structures and finally the fluid layer is dominated by numerous vortices. These are the stages of a time transition that develop progressively from a non-rotating to a rotating RBC. We will next investigate and show each of the transient behaviours by a quantitative approach.

3. Emergence of concentric convection roll structures

3.1. *Types of convection roll structures*

Imposing a rotation to an RBC flow, thermally coherent structures such as thermal plumes as appeared in figures 3 and 4 disintegrate due to the intense viscous dissipation of the rotation and the centrifugal forces. Mixing of the fluid in the azimuthal direction is shown as red and blue swirls which represent thermal plumes. The flow state can be considered as that of a stage in the spin-up of a fluid at rest without any thermal force imposed. Toroidal convection rolls appear progressively from the sidewall as shown in figures 3 and 4. The emergence of these ring structures was previously reported by Boubnov & Golitsyn (1986), Vorobieff & Ecke (1998), Zhong *et al.* (2010) and Ravichandran & Wettlaufer (2020). Considering these earlier reports, the ring structures appear regardless of the boundary conditions, namely, both in open to the air (slip) and enclosed (no-slip) vessels. In addition, the vessel geometry is not significant for the ring formation as the ring formations were observed both in rectangular (Boubnov & Golitsyn 1986; Zhong *et al.* 2010; Ravichandran & Wettlaufer 2020) and cylindrical vessels (Boubnov & Golitsyn (1986), Vorobieff & Ecke (1998) and the present study). The fluid vessels used in the earlier work were narrower ($0.656 \leq \Gamma \leq 2.00$) than those of the present study ($\Gamma = 2.00$ and 4.75), however, similar transient events were observed in the present conditions.

Vertical fluid motions are restricted in the spin-up process, except for the Stewartson layer formed at the sidewall and the centre of the fluid layer. The convection rolls may be induced by the vertical fluid transports carried out in the Stewartson layers at the sidewalls, as the layers transport hot and cold fluids at the bottom and top boundaries. Furthermore, the centrifugal force may influence the roll formation, as lower density (hot) and higher density (cold) fluids are transported towards the centre and the sidewall due to centrifugal effects.

In addition to the ring structures shown in figure 3, another type of concentric convection roll, a spiral structure, was identified. For a comparison of these two types of roll structures, figure 5 shows original images of ring (5*a*) and spiral (5*c*) structures, and the corresponding azimuthally extended images are in panels (*b*) and (*d*). The spiral-type rolls have not been reported in the previous work except for Boubnov & Golitsyn (1986); they noted that various roll patterns such as spirals or lemniscate-like structures were formed in eccentric arrangements between the centre of the fluid layer and the rotational axis, even though they did not provide any clear explanations. The two types of roll structures are formed in the same smaller cylinder $\Gamma = 2.00$ at the same Ra number $Ra = 2.0 \times 10^6$ with a slight difference in Ta values $Ta = 1.0 \times 10^7$ and 3.0×10^7. The types of rolls at all the explored parameters are summarized and detailed in figure 6. All the rolls are categorized into the ring and spiral types, and plotted with circles and diamonds, and for the smaller Γ and the larger Γ cases plotted as filled and open markers, respectively. Ring structures have a propensity to be formed at the lower Ra values and relatively higher Ta values. In addition, they are easily formed in the smaller cylinder $\Gamma = 2.00$ when compared with the larger cylinder $\Gamma = 4.75$.

Suppose the present system is a vertical symmetry, it may be not possible to observe the spiral-type rolls, as the centrifugal forces work as radially isotropic forces, and this situation always yields down-welling flows at the sidewall. Accordingly, a vertical asymmetry that provides an unbalance in the fluid deformation for forming the rolls, can be considered as one of the possible mechanisms to explain the presence of the spiral-type rolls. The present study performs experimental investigations, and we can deduce that there is a non-Oberbeck–Boussinesq (NOB) effect to generate a vertical asymmetry, as the effect may appear in the set temperature differences of $\Delta T = 2.2$ and 11.1 K for

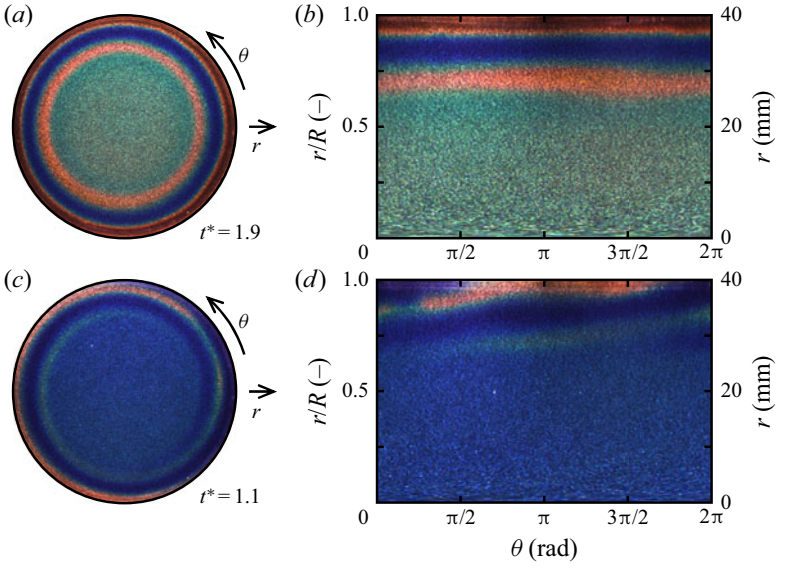

Figure 5. Two types of concentric roll structures observed in the smaller cylinder $\Gamma = 2.00$ at $Ra = 2.0 \times 10^6$: (*a*) ring type ($Ta = 3.0 \times 10^7$) and (*b*) its azimuthally extended image, and (*c*) spiral type ($Ta = 1.0 \times 10^7$) and (*d*) its azimuthally extended image.

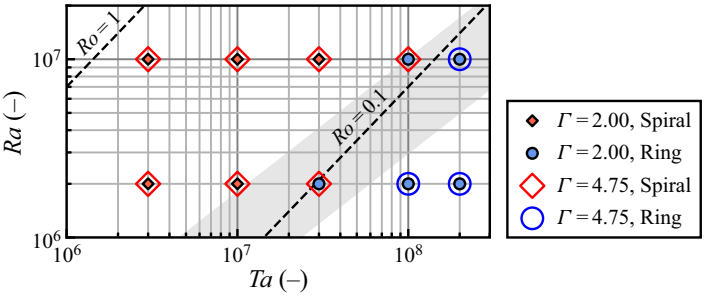

Figure 6. Regime diagram showing the types of convection roll structures which emerged soon after imposing the rotation. Small symbols indicate the plots for $\Gamma = 2.00$ and large symbols indicate the plots for $\Gamma = 4.75$. Spiral types and ring types are represented by red diamonds and blue circles. Dashed lines indicate $Ro = 1$ and 0.1 with $Pr = 7$. The grey shaded region is the crossover range of the boundary layer thicknesses predicted by King, Stellmach & Aurnou (2012).

$Ra = 2.0 \times 10^6$ and 1.0×10^7 (Gray & Giorgini 1976). Horn & Shishkina (2014) provided direct numerical simulations for rotating RBC in water with a NOB condition and showed that the thicknesses of the thermal boundary layers at the top and bottom change drastically at $Ro \sim 0.14$, due to a crossover in the thicknesses of the thermal and viscous boundary layers. For $Ro \gtrsim 0.14$, the thermal boundary layer at the top is always thicker than that at the bottom, and this relation reverses for $Ro \lesssim 0.14$. For the larger Ro conditions, the thermal boundary layer at the bottom is easily unstabilized compared with the smaller Ro conditions and the convection flows can develop from both the top and bottom plates, whereas the thermal boundary layer at the top is easily unstabilized for the smaller Ro conditions. King *et al.* (2012) observed that the crossover in the thicknesses of the boundary layers occurs somewhere between $6 \lesssim RaEk^{3/2} \lesssim 20$, or expressed in terms

of Ta, it should exist in the range $3 \lesssim RaTa^{-3/4} \lesssim 10$. The predicted range is shaded as grey in figure 5, and it is noteworthy that the range roughly agrees with the border for separating the two types of rolls at $Ro \sim 0.1$, indicated by a dashed line in the figure.

Furthermore, the aspect ratio of the fluid layer Γ is another factor for determining the roll type. The present study uses the cylindrical vessel of $\Gamma = 2.00$ and 4.75, which is larger than the one ($\Gamma = 1$) used in Vorobieff & Ecke (1998). The larger aspect ratio may easily provide a vertical asymmetry to the system, as the longer circumference of the vessel is hard to synchronize in the fluid motions even with a strong centrifugal force. The dependence on the aspect ratio might not be possible to ignore, and rather more significant than the NOB effect for considering this kind of pattern formation problem. Incorporating the discussions above, the balance of the centrifugal force and the degree of vertical symmetry of the top and bottom boundary layers are considered as the determinant of the roll types: the conditions with sufficiently strong centrifugal forces compared with the vertical disturbances originating from the vertical asymmetry of the boundary layers can form the ring-type rolls.

3.2. *Characteristics of the concentric roll structures*

To observe the formation of concentric convection rolls quantitatively, flow fields were obtained by PIV analysis for both the horizontal and vertical visualization experiments. As well as for the vertical cross-section measurements, in the present case PIV analysis is possible for particle images obtained by the horizontal TLC measurements because of the sufficiently small and well distributed TLC particles, and the high resolution digital images with 2000 pixels to the fluid layer diameter of $2R = 80$ or 190 mm. Examples of the flow fields in the situation where the roll formation has taken place in the horizontal ($z = 0.5H$) and the vertical ($y = 0.0$) cross-sections are shown in figure 7. For the PIV analysis, velocity vectors are obtained at every 1 mm in both directions of the Cartesian coordinates, and one of two vectors (black arrows) are displayed in any direction in figure 7. The arrow sizes are adjusted in each panel regardless of the magnitude of the velocity for clearer visibility. The velocity fields in the horizontal cross-section (figure 7*a*) and those in the vertical cross-section (figure 7*b*), are obtained with data for two different individual experimental runs, and thus the extracted different snapshots of the flow fields are, strictly speaking, different. The colour contours in figure 7 show the out-of-plane vorticities; the vorticity in z-direction $\omega_z = \partial u_y/\partial x - \partial u_x/\partial y$ (figure 7*a*), and that in y-direction $\omega_y = \partial u_x/\partial z - \partial u_z/\partial x$ (figure 7*b*). At $t^* = 1.00$ the ω_z in the horizontal plane is large due to momentum transfer from the sidewall. In the vertical plane, the interior core region is highly disorganized with small coherent structures of ω_y, while there are boundary layers at the sidewall. At $t^* = 1.50$ in the horizontal plane, the core region with negative ω_z values is smaller, and a prominent positive ω_z ring appears at the vicinity of the sidewall. Correspondingly, in the vertical plane the roll structures expressed as vorticity distributions organized in the z-direction emerge at the vicinity of the wall, while the core region is still disorganized. At $t^* = 2.00$ formation of convection rolls has progressed away from the wall towards the centre of the fluid layer. This is clearly the case both in the horizontal and vertical planes, as shown by the alignment of alternate positive and negative vorticity in the radial directions.

To investigate the concentric convection roll structures quantitatively, each roll structure is necessary to be fully established from the velocity fields. Roll boundaries can be identified by the directions of vertical flows u_z, as developed thermal convection should have vertical flows in one direction along with the fluid layer depth (z-direction). For this

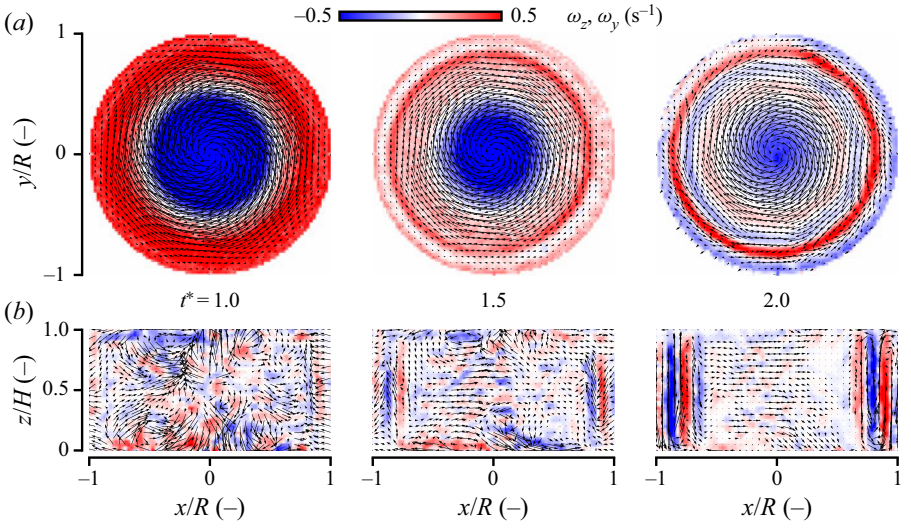

Figure 7. Instantaneous velocity and vorticity fields obtained by PIV analysis for $\Gamma = 2.00$, $Ra = 2.0 \times 10^6$ and $Ta = 3.0 \times 10^7$ in the situation of roll formation: (*a*) u_x–u_y vectors (black arrows) plotted on the out-of-plane vorticity ω_z (coloured contours) at $z = 0.5H$; (*b*) u_x–u_z vectors (black arrows) plotted on the out-of-plane vorticity ω_y (coloured contours) at $y = 0.0$. Time advances from left to right and is indicated between panels (*a*) and (*b*). One of two vectors is plotted in any direction for visibility and the vector sizes are adjusted in each panel to enhance clarity.

reason the vertically averaged vertical velocity $\langle u_z \rangle_z$ is a useful indicator to identify the vertical flows, and it is calculated as

$$\langle u_z \rangle_z = \frac{1}{H} \int_0^H u_z(x, z)\, \mathrm{d}z, \tag{3.1}$$

in the PIV results of the vertical cross-section shown in figure 7. An example of the radial profile of a calculated $\langle u_z \rangle_z$ for the case of $\Gamma = 2.00$, $Ra = 2.0 \times 10^6$ and $Ta = 3.0 \times 10^7$ is shown in figure 8. Here $\langle u_z \rangle_z$ is normalized by the free-fall velocity $U_f = \sqrt{g\beta\Delta TH}$. The time evolution of the profile is shown using colour coding. Clear wavy patterns can be seen extending radially outward ($|x| \gtrsim R/2$) and there are some zero-crossing points at which $\langle u_z \rangle_z = 0$, as indicated by the diamonds in the figure. These zero crossings are regarded as the centres of the roll structures, and the local maxima and local minima of $\langle u_z \rangle_z$ correspond to the roll boundaries. The zero-crossing points and the local maxima/minima are determined by the spline interpolation on the profile of $\langle u_z \rangle_z$. Boundary layers at the two sidewalls are marked in the darkest grey. Each roll structure and the corresponding thickness δ_{roll} may be considered as the distance between the local maxima and local minima, and are identified individually by the painted regions with different lighter greys inward in figure 8. The thickness of rolls are numbered in order from the wall towards the centre as ± 1, ± 2, ± 3 and these are indicated at the bottom in figure 8. The result shown in figure 8 is the case for the ring-type rolls, however, the cases for the spiral-type rolls are also possible to analyse in the same manner. The zero-crossing points and the local minima/maxima seem to be fixed, at least during $t^* = 1.0$–2.0, and behave as nodes and antinodes in figure 8. Expressed differently, the roll structures do not widen in thickness or move radially as time elapses from their formation until they collapse into azimuthally aligned vortical structures, as shown in figures 3 and 4.

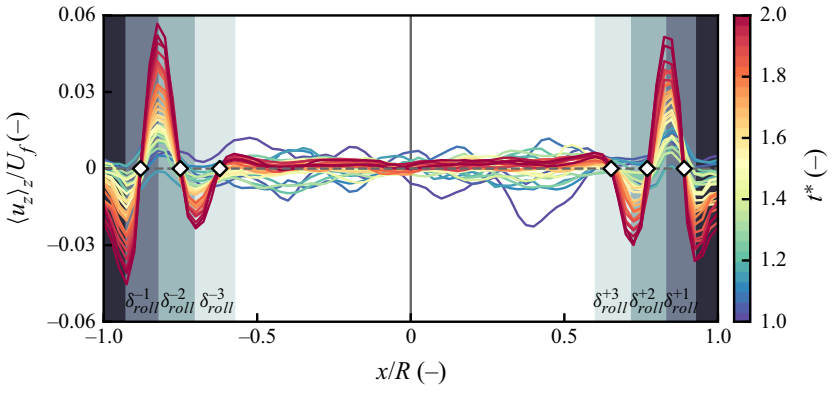

Figure 8. Horizontal profiles of the vertically averaged vertical velocity $\langle u_z \rangle_z$ in the vertical cross-section $y = 0.0$ with $\Gamma = 2.00$, $Ra = 2.0 \times 10^6$ and $Ta = 3.0 \times 10^7$. Here $\langle u_z \rangle_z$ is normalized by the free-fall velocity U_f. Time evolution of the profiles is displayed by the colour coding. Zero-crossing points of the profiles are marked by diamonds. The regions nearby two sidewalls painted in the darkest grey are the sidewall boundary layers. Other regions painted in grey being gradually lighter inward indicate the thickness of individual roll structures δ_{roll} which can be determined by the distance between the local maxima and minima of $\langle u_z \rangle_z$.

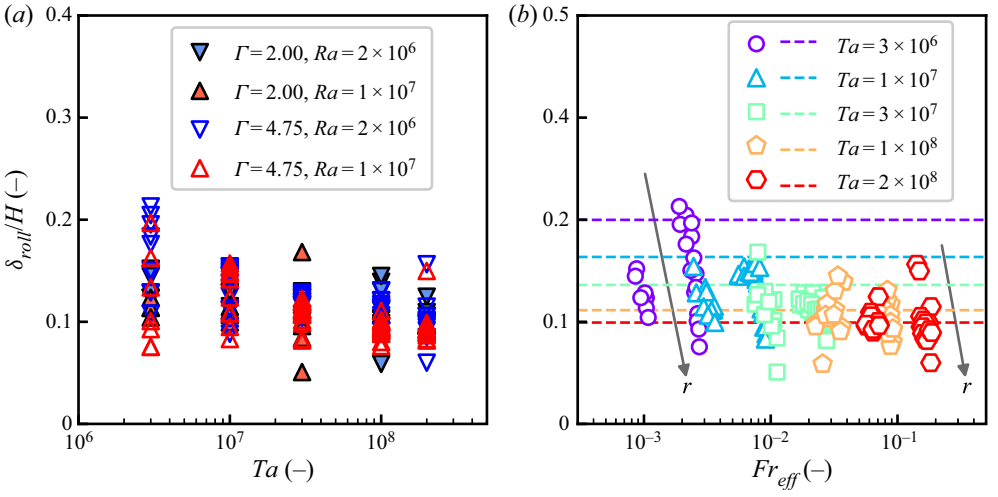

Figure 9. Roll thickness δ_{roll} measured for all the explored parameters. (*a*) Here δ_{roll}/H is plotted with Ta values. Filled and open symbols indicate the case with $\Gamma = 2.00$ and $\Gamma = 4.75$, respectively. Inverse and regular triangles are for $Ra = 2.0 \times 10^6$ and $Ra = 1.0 \times 10^7$, respectively. (*b*) Here δ_{roll}/H is plotted with effective Fr values Fr_{eff}. Circles, triangles, squares, pentagons and hexagons indicate $Ta = 3.0 \times 10^6$, 1.0×10^7, 3.0×10^7, 1.0×10^8 and 2.0×10^8, respectively. The horizontal dashed lines are the theoretical values $2.4HTa^{-1/6}$ estimated by Cheng *et al.* (2018). The markers and dashed lines are individually colour coded with Ta values. Grey arrows are approximate guides indicating the radial position of each convection roll.

Considering the negligibly small time variations of the roll structures, the roll thickness δ_{roll} can be estimated from the distance between the local maxima/minima on temporally averaged profiles of $\langle u_z \rangle_z$ for a specific duration. In figure 9(*a*), the estimated δ_{roll} including $\delta_{roll}^{\pm 1}$, $\delta_{roll}^{\pm 2}$, $\delta_{roll}^{\pm 3}$ …, for all the explored parameters are summarized. The roll thicknesses δ_{roll} normalized by the fluid layer depth H distribute around 0.1–0.2, showing the rolls to

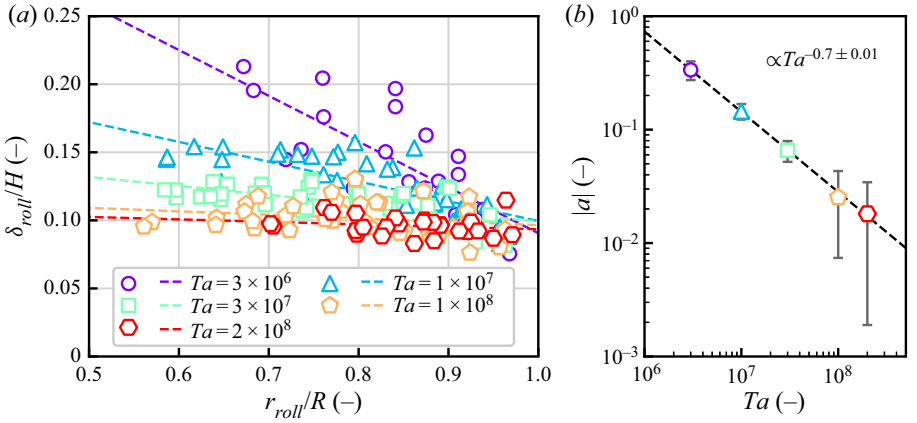

Figure 10. (*a*) Relation between the roll thickness δ_{roll} and the corresponding radial position. Circles, triangles, squares, pentagons and hexagons indicate $Ta = 3.0 \times 10^6$, 1.0×10^7, 3.0×10^7, 1.0×10^8 and 2.0×10^8, respectively. Dashed lines show the least-squares fits of linear regressions ($\delta_{roll}/H = ar_{roll}/R + b$) for each Ta condition. The markers and dashed lines are individually colour coded with Ta values. (*b*) The Ta dependence of the absolute value of slopes to the fitting lines $|a|$. The slopes in panel (*a*) become flatter with increase in Ta proportional to $Ta^{-0.7\pm0.01}$ as guided by the dashed line. Standard deviations for $|a|$ in the fitting of panel (*a*) are shown as error bars.

be narrow and tall structures. There appear to be no regular changes in δ_{roll} for the Ra and Ta values in figure 9(*a*).

As δ_{roll} is not clearly described by either of the Ra or Ta values, another determinant for δ_{roll} should exist, one that is independent of thermal buoyancy and Coriolis forces. The centrifugal force may be a possible principal influence since it is a radially isotropic force forming the concentric structures as discussed in § 2.3. One candidate for understanding the effect of the centrifugal force could be the Froude number Fr. The effective Froude number is defined as $Fr_{eff} = r_{roll}\Omega^2/g$, where r_{roll} indicates the radial position of the roll centre (zero-crossing point of $\langle u_z \rangle_z$). In figure 9(*b*), δ_{roll} is plotted with Fr_{eff}. With the increase of Fr_{eff} (the centrifugal effect), δ_{roll} gradually decreases, and the deviations of δ_{roll} with smaller Fr_{eff} are larger. Furthermore, δ_{roll} for the same Ta conditions decreases with increases in Fr_{eff}. Taken together, the roll thickness becomes narrower as the roll forms radially outward. For comparison, the critical wavelength at the onset of the rotating RBC, $2.4HTa^{-1/6}$, derived by Cheng *et al.* (2018) using the linear stability analysis are plotted with the dashed horizontal lines. In particular the measured δ_{roll} for the larger Ta cases are slightly smaller than what would be expected from the previous reports.

Differences in r_{roll} result in quite large deviations in δ_{roll} as guided by the grey arrows in figure 9(*b*); δ_{roll} is wider at the interior of the fluid layer (see figure 8). The relation between δ_{roll} and r_{roll} is plotted in figure 10(*a*). Here the radial positions r_{roll} are normalized by the fluid layer radius R, and results in both of the fluid layers of $\Gamma = 2.00$ and 4.75 are plotted. Regardless of Γ and Ra values, δ_{roll} increases as roll structures form at the interior of the fluid layer, even when large deviations exist, especially for the smaller Ta conditions. This trend can be fitted roughly by the linear regressions in the form of $\delta_{roll}/H = ar_{roll}/R + b$ individually for each Ta condition, and are shown as dashed lines in figure 10(*a*). The slopes are steeper for smaller Ta values, and gradually become flatter with increases in Ta values, even with the large deviations due to a fixed observation cross-section at $y = 0$. This Ta dependence of the absolute values of the slopes $|a|$ is shown in figure 10(*b*). Standard deviations for $|a|$ in the linear regressions of figure 10(*a*) are shown as error bars.

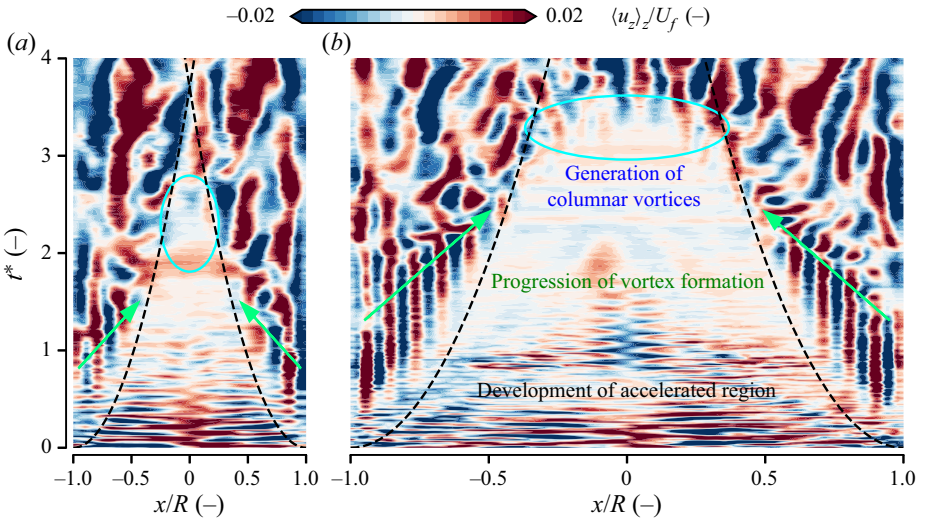

Figure 11. Time evolution of the vertically averaged vertical velocity $\langle u_z\rangle_z$ for $Ra = 1.0 \times 10^7$ and $Ta = 3.0 \times 10^7$ at different aspect ratios: (*a*) $\Gamma = 2.00$ and (*b*) $\Gamma = 4.75$. Time elapses from bottom to top. Dashed lines indicate the development of accelerated region due to the fluid viscosity from the sidewall expressed as $\delta_v \propto \sqrt{\nu t}$ with arbitrary scaling factors. Arrows from the wall to the centre indicate the progression of the vortex formation induced by the KH instability to be discussed in § 4. Regions enclosed by ellipses indicate the generation of the columnar vortices due to separation of the thermal boundary layer.

For the explored Ta parameters, $|a|$ is proportional to $Ta^{-0.7\pm0.01}$ as indicated by the dashed line. Hence, δ_{roll} can be approximately estimated from only the Ta values and the formation radius r_{roll}. Vorobieff & Ecke (1998) mentioned that the radial positions of the first hot rings (up-welling streams), r_{roll} in the present notation, are always seen at $r_{roll} \sim 3R/4$ in the cylinder with $\Gamma = 1$ regardless of the experimental parameters. The first position of roll formation is, however, not essential because this is automatically determined by the roll thickness δ_{roll} first formed at the vicinity of the sidewall. Thus, the present study using rather larger Γ than that of Vorobieff & Ecke (1998), shows larger radial positions ($r_{roll}/R > 0.75$) at which the first roll is formed.

3.3. *Wall-to-centre propagation of convection roll formation*

Convection rolls remain stable from their emergence until the appearance of azimuthal distortions as detailed in § 4. In this section, we investigate the progress of roll generation from the sidewall towards the centre of the fluid layer shown in figures 3, 4 and 7. Spatiotemporal extended images of radial profiles of $\langle u_z\rangle_z$ at $Ra = 1.0 \times 10^7$ and $Ta = 3.0 \times 10^7$ with changing Γ are shown in figure 11 to better understand the temporal evolution of the roll formation. The colour contour shows values of $\langle u_z\rangle_z$ normalized by the free-fall velocity U_f. The result of $\Gamma = 2.00$ is shown in figure 11(*a*) and that of $\Gamma = 4.75$ in figure 11(*b*). Positive and negative values of $\langle u_z\rangle_z$ appear from the sidewall ($|x|/R \sim 1$) alternately and are shown as red and blue organized columns. These columns in figure 11 qualitatively express the convection roll structures. Considering the emergence points of the organized columns, it is obvious that the rolls form in order from the sidewall and migrate towards the centre of the fluid layer. As a reason for this wall-to-centre progression of the roll formation, it is plausible to consider the development of the accelerated region from the sidewall due to the fluid viscosity. For the discussion here we simply assume that

the increase of the thickness of accelerated region at sidewall δ_ν can be described by that of the two-dimensional (2-D) Rayleigh problem (Stokes' first problem); the accelerated region develops as $\delta_\nu \propto \sqrt{\nu t}$. For reference, the time variations of δ_ν with arbitrary scaling factors is plotted as black dashed lines in figure 11. The time of appearance of the roll structures qualitatively match the development of the accelerated region. That would allow the assumption that the roll structures form in the regions where rigid-body rotation has been achieved.

Sometime after the roll formation, the red and blue columns in figure 11 start to fluctuate and become disorganized, which is apparent from the discontinuity of the columns along the time (vertical) axis. As detailed in § 3.2, the convection roll thickness and positions change little until their collapse (at $t^* \sim 1.2$ for the outer rolls in the displayed cases). In figures 7 and 11, the inner region where no rolls form appear to be organized by small, turbulent structures during the wall-to-centre progression of the roll formation. Viscous dissipation in the interior region, at which the rigid-body rotation has not been achieved, can be considered as too strong for the separation of the thermal boundary layer. This results in the creation of convection rolls being suppressed, and only few organized coloured columns are seen at the interior region in figure 11.

4. Formation of azimuthally aligned vortices

4.1. *Instability to induce vortical structures*

As reported elsewhere, concentric roll structures, rings or spirals, formed at the early stage of the spin-up of the thermal convection subsequently collapse into vortical structures as shown in figures 3 and 4. Boubnov & Golitsyn (1986) indicated the cause of the emergence of these azimuthally aligned vortices as instances of KH instability. Vorobieff & Ecke (1998) showed this by PIV analysis. Zhong *et al.* (2010) also conducted PIV analysis to provide a quantitative explanation of the emergence of the KH instability. Intuitively these explanations are plausible; however, it is necessary to show proof of the KH instability such as in the existence of inflection points on the radial profiles of the azimuthal velocity, something which has not been reported as yet. In the present study the spatial resolution of the PIV grids is sufficiently fine (1 mm) to resolve the vortical structures induced by the KH instability $O(10^1$ mm). Examples of velocity vector fields both in the horizontal and the vertical slices at the time around the emergence of the vortical structures are shown in figure 12. As in figure 12(*a*), rings of different sign vorticity are aligned alternately from the sidewall to the centre at $t^* = 2.20$. The fluctuations of the rings increase with radial amplitudes and grow gradually into vortical structures at $t^* = 2.20$ and 2.50. This fluctuation pattern propagates in the azimuthal direction from the first fluctuating position (right-hand side in the figure) and eventually azimuthally aligned vortices are formed at $t^* = 2.50$ and 3.00. In the vertical cross-section, it is possible to see vertically organized patterns of the vorticity ω_y at $t^* = 2.20$. Away from the outer regions forming the convection rolls, fluid is stagnant in the interior region. With time elapsed, the flow directions vary within the rolls expressed by the same signed vorticity columns. These results indicate that the convection roll structures collapse into vortices aligned in the azimuthal direction. To prove the occurrence of the KH instability, radial inflection points $\tilde{r}$ of azimuthal velocity $u_\theta = -u_x \sin\theta + u_y \cos\theta$, where $\partial^2 u_\theta / \partial r^2 = 0$, should be explored quantitatively. For this, using the azimuthal velocity in an absolute system $U_\theta = u_\theta + r\Omega$ is appropriate. This is because the KH instability occurs in the absolute system with a small perturbation affecting the rigid-body rotation. In the horizontal cross-section, azimuthally

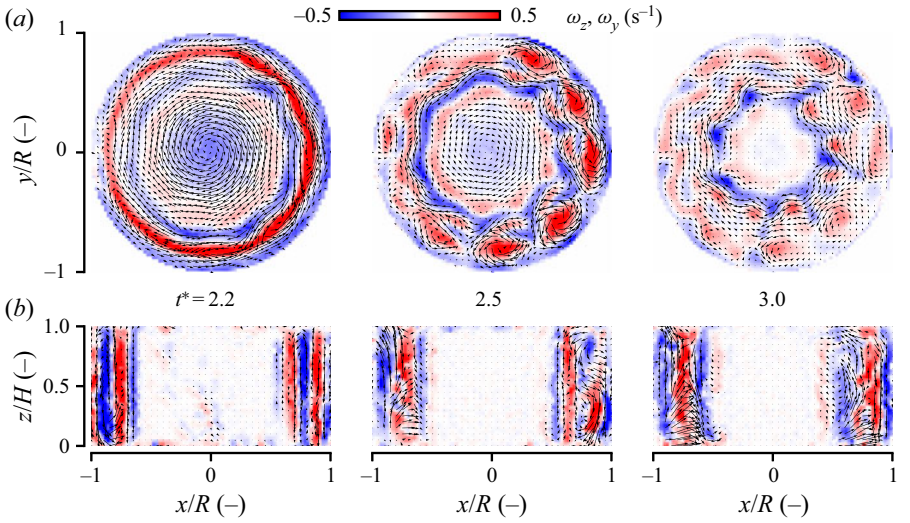

Figure 12. Velocity and vorticity fields obtained by PIV analysis for $\Gamma = 2.00$, $Ra = 2.0 \times 10^6$ and $Ta = 3.0 \times 10^7$ in the situation with vortex formation: (*a*) u_x–u_y vectors (black arrows) plotted on the out-of-plane vorticity ω_z (coloured contours) at $z = 0.5H$; (*b*) u_x–u_z vectors (black arrows) plotted on the out-of-plane vorticity ω_y (coloured contours) at $y = 0.0$. Time elapses from left to right and is indicated between panels (*a*) and (*b*). One of two vectors is plotted in any direction for visibility and the vector sizes are adjusted in each panel to enhance clarity.

averaged profiles of the azimuthal velocity $\langle U_\theta \rangle_\theta$ is calculated according to

$$\langle U_\theta \rangle_\theta = \frac{1}{2\pi} \int_0^{2\pi} U_\theta(r, \theta)\, \mathrm{d}\theta, \tag{4.1}$$

and shown in figure 13(*a*). In the calculation of U_θ, the velocity vectors in the Cartesian grid are assigned to the nearest one-dimensional radial array made every 1 mm from $r = 0$ to R. This conversion involving the azimuthal averaging improves the apparent velocity resolution of the PIV, and makes it possible to obtain the second derivative of $\langle U_\theta \rangle$ for indicating inflection points. Furthermore, slight differences in velocity profiles originating from the two different roll types, ring and spiral, become negligible by this azimuthal averaging, and the two types can be treated equally in the subsequent analysis. In figure 13(*a*) $\langle U_\theta \rangle_\theta$ is normalized by the sidewall velocity $R\Omega$ and represented as U_θ^*. Also, the radial coordinate r is normalized by the cylinder radius R and represented as r^*. The curves of $\langle U_\theta \rangle_\theta$ in the figure eventually approach linearity with a slope of Ω (indicated as the dashed grey line), and thus the flow can be considered to approach rigid-body rotation. Especially at the vicinity of the sidewall $r^* \sim 1$, U_θ^* matches well with the velocity of the rigid-body rotation at $t^* = 3.0$. For comparison, azimuthally averaged velocity profiles in the rotational system $\langle u_\theta \rangle_\theta = \langle U_\theta \rangle_\theta - r\Omega$ are also shown in figure 13(*b*). Here, a similar normalization to U_θ^* is adopted for $\langle u_\theta \rangle_\theta$ and is represented as u_θ^*. Unlike in figure 13(*a*), the curves in figure 13(*b*) start to fluctuate especially around the sidewall when the time approaches $t^* \sim 3.0$. By differentiating U_θ^* by r^*, it is possible to obtain the slope of U_θ^*, as shown in figure 13(*c*). The dashed grey line in the figure shows $\mathrm{d}U_\theta^*/\mathrm{d}r^* = 1$ representing $U_\theta/r = \Omega$. Furthermore, the second derivative of U_θ^* with r^* displayed in figure 13(*d*) proves that there are inflection points as indicated by the diamonds, where $\mathrm{d}^2 U_\theta^*/\mathrm{d}r^{*2} = 0$. In the displayed condition in figure 13, there are three inflection points,

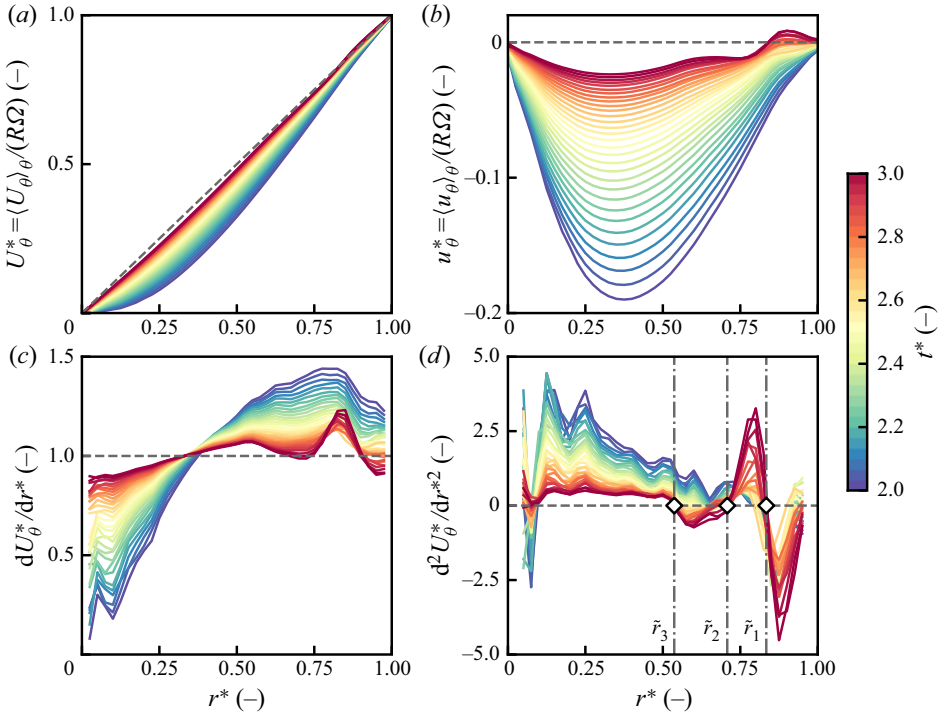

Figure 13. Radial profiles of velocity and its derivatives obtained by PIV analysis for $\Gamma = 2.00$, $Ra = 2.0 \times 10^6$ and $Ta = 3.0 \times 10^7$ at $z = 0.5H$: (*a*) the averaged azimuthal velocity U_θ^* in the absolute coordinate system plotted with the rigid-body rotation velocity profile (dashed grey line); (*b*) the averaged azimuthal velocity u_θ^* in the rotational (PIV) coordinate system plotted with the rigid-body rotation velocity profile (dashed grey line); (*c*) the first derivative of U_θ^* differentiated by the non-dimensional radius r^* indicating the slope of panel (*a*) plotted with the system angular velocity (dashed grey line); (*d*) the second derivative of U_θ^* differentiated by r^*. Zero-crossing points $\tilde{r}$ indicated as diamonds correspond to the inflection points of U_θ^*. Three inflection points indicated by the vertical dashed-dotted lines are numbered in order from the sidewall. Time evolution is displayed using colour coding.

and the radial positions of the inflection points $\tilde{r}$ are found to correspond to the positions of up-welling and down-welling flows, i.e. the roll boundaries. These results provide proof for the occurrence of the KH instability from the typical characteristics of the velocity profiles.

4.2. *Wavenumbers and wavelengths of vortical structures*

Because the vortical structures originating from the KH instability are generated along the boundaries of concentric rolls, the wavenumber of the KH instability can be determined from the number of vortices formed along the circumferences on the inflection points $r = \tilde{r}$. As shown in figure 12(*a*), a vortex can be identified from the spatial distributions of ω_z showing azimuthally aligned patterns at $t^* = 2.50$ and 3.00. To count the number of vortices, a fast Fourier transform (FFT) analysis for the azimuthal profiles of ω_z along the circumferences at $r = \tilde{r}$ is useful, because the prominent power spectrum is expected to appear at the wavenumber corresponding to the number of vortices. In figure 13(*d*), three inflection points are identified as indicated by diamonds, and the radial positions of the inflection points are labelled in order as $\tilde{r}_1$, $\tilde{r}_2$ and $\tilde{r}_3$ from the wall towards

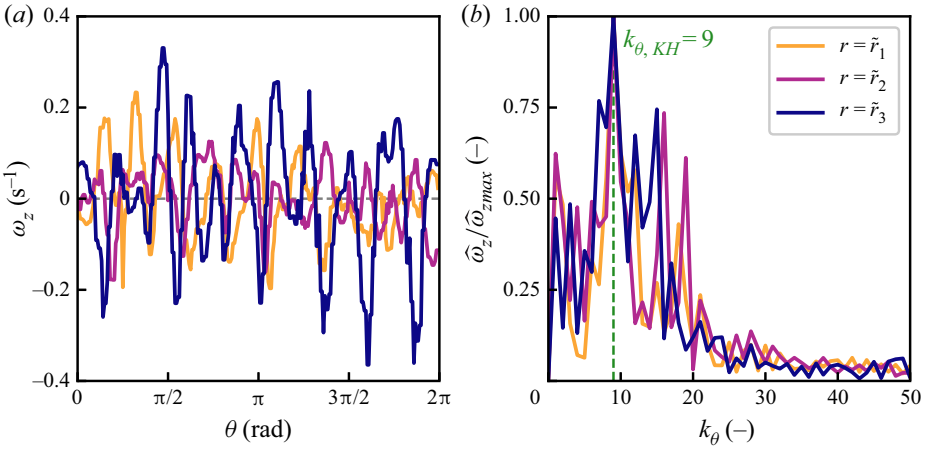

Figure 14. (*a*) Azimuthal profiles of ω_z along the circumferences at the three inflection points $r = \tilde{r}_1$, $\tilde{r}_2$ and $\tilde{r}_3$ and (*b*) the corresponding power spectra $\widehat{\omega_z}$ obtained by the FFT analysis with $\Gamma = 2.00$, $Ra = 2.0 \times 10^6$ and $Ta = 3.0 \times 10^7$. The power spectra are normalized by the maximum values of each power spectrum $\widehat{\omega}_{zmax}$ for better visibility. Vertical dashed line is the azimuthal wavenumber $k_\theta = 9$ showing the maximum values of each power spectrum $\widehat{\omega}_{zmax}$, and is regarded as the wavenumber of the KH instability $k_{\theta,KH}$.

the centre. The three azimuthal profiles of ω_z along the circumferences at $r = \tilde{r}$ are shown in figure 14(*a*), and the corresponding power spectra $\widehat{\omega_z}$ obtained by an FFT analysis are shown in figure 14(*b*). In figure 14(*b*) the power spectra are normalized by the various maximum values $\widehat{\omega}_{zmax}$ for better visibility. The azimuthal wavenumbers k_θ which show $\widehat{\omega}_{zmax}$ can be regarded as the wavenumber of the KH instability $k_{\theta,KH}$, and are identical to $k_\theta = 9$ for all the inflection points.

The wavenumbers of the KH instability $k_{\theta,KH}$ for all the explored parameters are shown in figure 15(*a*). The larger aspect ratio $\Gamma = 4.75$ yields larger values of $k_{\theta,KH}$ than those in $\Gamma = 2.00$. For both the Γ values, $k_{\theta,KH}$ decreases monotonically with increases in the Ro values. The decreasing tendencies were approximated by the least-squares method of $k_{\theta,KH} = 4.4Ro^{-0.35}$ ($\Gamma = 2.00$) and $k_{\theta,KH} = 13.2Ro^{-0.37}$ ($\Gamma = 4.75$), and are shown by the dashed and dashed-dotted lines, respectively, in figure 15(*a*). These approximations suggest that $k_{\theta,KH}$ depends on only the Ro values, regardless of the radial positions and thicknesses of the rolls.

Next we will consider a reason for the Ro dependence of $k_{\theta,KH}$. According to Drazin & Reid (2004), in the classical problem setting of the KH instability considering vertically stratified fluids with different densities under the influence of gravity, the wavenumber k_{KH} of the KH instability is expressed as

$$k_{KH} = \frac{g\left(\rho_1^2 - \rho_2^2\right)}{\rho_1\rho_2\left(U_1 - U_2\right)^2}, \tag{4.2}$$

with U_1 and U_2 the horizontal velocities at the density interface of two stratified fluids with densities of ρ_1 and ρ_2. For the discussion on the present experimental results we simply assume that the KH instability happens in radially stratified fluids with different densities under the influence of centrifugal forces, the gravitational acceleration g in the classical KH problem can be replaced by the centrifugal acceleration $r\Omega^2$. With this, the azimuthal

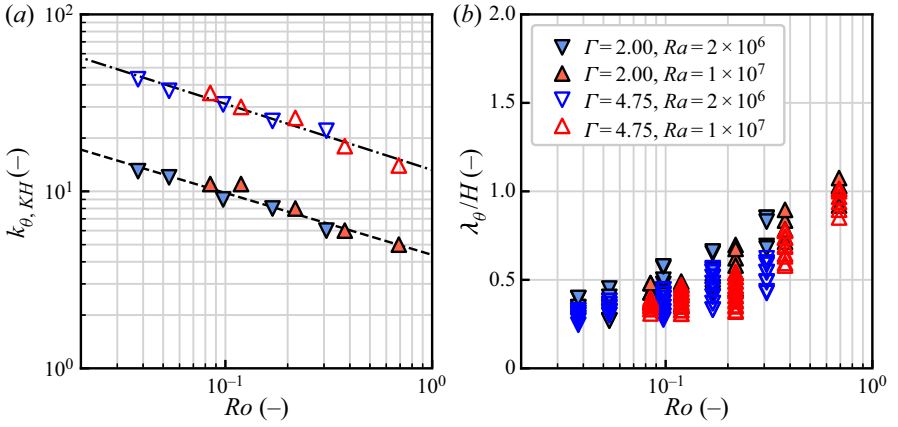

Figure 15. (*a*) Wavenumber of the KH instability $k_{\theta,KH}$ and (*b*) the azimuthal wavelength of the KH instability λ_θ for all the inflection points. Filled and open symbols indicate the case with $\Gamma = 2.00$, and with $\Gamma = 4.75$, respectively. Inverse and regular triangles are for $Ra = 2.0 \times 10^6$ and $Ra = 1.0 \times 10^7$, respectively. The dashed and the dashed-dotted lines displayed in panel (*a*) are the least-squares fits of $k_{\theta,KH} = 4.4Ro^{-0.35}$ and $k_{\theta,KH} = 13.2Ro^{-0.37}$, respectively, for $\Gamma = 2.00$ and 4.75.

wavenumber $k_{\theta,KH}$ of the KH instability can be written as

$$\frac{k_{\theta,KH}}{2\pi r} = \frac{r\Omega^2\left(\rho_1^2 - \rho_2^2\right)}{\rho_1\rho_2\left(U_{\theta 1} - U_{\theta 2}\right)^2}, \tag{4.3}$$

where $U_{\theta 1}$ and $U_{\theta 2}$ are the azimuthal velocities in each layer of the two fluids with densities of ρ_1 and ρ_2. Under the Boussinesq approximation, the density difference in the radial direction can be represented by the temperature difference ΔT in the radial direction as $|\rho_1 - \rho_2| = \Delta\rho = \rho_0\beta\Delta T$, where ρ_0 is the reference density. Considering the meridional circulation of convection rolls, ΔT can be replaced by an Ra value because the temperature difference in the radial direction and that in the vertical direction are identical. This allows the part related to the density in (4.3) to be expressed by an arbitrary function of Ra as $\mathcal{F}(Ra)$. The azimuthal velocity difference can be also rewritten as $|U_{\theta 1} - U_{\theta 2}| = |(r + \Delta r)\Omega - r\Omega| = \Delta r\Omega$ because the instability happens in the situation of the rigid-body rotation. Accordingly, suppose Δr is equivalent to the roll thickness δ_{roll}, and (4.3) can be modified to

$$k_{\theta,KH} \propto r^2\mathcal{F}(Ra)\delta_{roll}^{-2}. \tag{4.4}$$

As mentioned in § 3.2, δ_{roll} is approximated by $\delta_{roll} \sim -Ta^\alpha r$, where α is a scaling index ($\alpha \sim -0.7$ in the present case as indicated in figure 9*b*). Incorporating all of the assumptions, the wavenumber is simply written as

$$k_{\theta,KH} \propto r^2\mathcal{F}(Ra)(Ta^\alpha r)^{-2} = \mathcal{G}(Ra, Ta). \tag{4.5}$$

The dependence of $k_{\theta,KH}$ on the radial position is cancelled out, and $k_{\theta,KH}$ can be expressed as an arbitrary function, $\mathcal{G}$, of Ra and Ta. For a specific Pr value, the Ra and Ta values can be replaced by the Ro value as shown in figure 15(*a*).

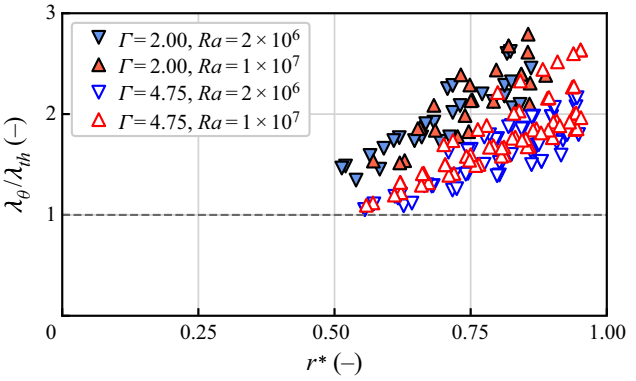

Figure 16. Radial distributions of the horizontal scale of the vortical structures as the azimuthal wavelength of the KH instability λ_θ normalized by the theoretically derived horizontal scale of the convection cell λ_{th} under an equilibrium state of rotating RBC by Sakai (1997). Filled and opened symbols are for the case with $\Gamma = 2.00$ and $\Gamma = 4.75$, respectively. Inverse and regular triangles indicate $Ra = 2.0 \times 10^6$ and $Ra = 1.0 \times 10^7$, respectively.

The azimuthal wavelength of the KH instability λ_θ, the horizontal scale of the vortical structures, can be calculated at each inflection point $\tilde{r}$ using $k_{\theta,KH}$ as

$$\lambda_\theta = \frac{2\pi\tilde{r}}{k_{\theta,KH}}, \tag{4.6}$$

and this is plotted in figure 15(*b*). In the figure, λ_θ increases as Ro values increase with considerable deviations, however. As mentioned above, $k_{\theta,KH}$ has a unique value independent of the radial position, and thus λ_θ decreases when moving radially inward into the fluid layer.

The deviations in each Ro value in figure 15(*b*) indicate the dependence of λ_θ on the radial position as shown in figure 16. Here the λ_θ values are normalized by the horizontal scale of the columnar vortices λ_{th} in an equilibrium state of the rotating RBC estimated theoretically by Sakai (1997). There, λ_{th} is derived as

$$\lambda_{th} = 4.6H\frac{\delta_t^2}{2\delta_t^2 + 2\delta_t\delta_E + \delta_E^2}Ra^{1/3}Ta^{-3/8}, \tag{4.7}$$

where δ_t and δ_E are the thickness of the thermal boundary layer and the Ekman layer, respectively. The applicability of λ_{th} in describing the experimental data has been confirmed (Sakai 1997; Noto *et al.* 2018, 2019; Fujita *et al.* 2020). In figure 16, λ_θ takes smaller values at more inner positions, but does not exceed λ_{th} even with the smallest cases around $r^* = 0.5$. The markers in figure 16 disappear at $r^* < 0.5$, at the intermediate radius of the fluid layer, as no distinct inflection points could be observed at $r^* < 0.5$. This is also apparent in figure 11 where the formations of convection rolls shown as the organized vertical columns is not present at $|x|/R < 0.5$. Here the λ_θ represents the length in the azimuthal direction regardless of that in the radial direction. As observed in figures 3, 4 and 12, the shapes of the vortices induced by the KH instability are elliptic at the vicinity of the sidewalls and closer to circular in radially farther inward positions of the fluid layer. This suggests that the wavelength of a KH instability is always larger than that of the columnar vortices formed in an equilibrium state of rotating RBC until the instability expires for $r^* < 0.5$.

4.3. *Wall-to-centre propagation of vortex formation*

The convection rolls maintain their structures for certain periods in the spin-up process and are broken because of the onset of the KH instability. This is expressed by the disappearance of the organized columns representing the convection rolls in figure 11. The onset of the KH instability and subsequent formation of the vortical structures progressively propagate from the sidewall towards the centre as indicated by green arrows in figure 11, and this trend is similar to the wall-to-centre progression of the roll formations detailed in § 3.3. As expressed by the shorter lengths of the organized columns at the internal positions in figure 11, the lifetime of convection rolls becomes shorter as the positions of the convection rolls face radially inward. Considering these results, it may be concluded that the vortex formation progresses faster than that of the convection roll formation.

This difference in the speed of progression of vortex and roll could be explained by the growth rate of the KH instability. The azimuthal wavenumber $k_{\theta,KH}$ of the KH instability is determined only by *Ra* and *Ta*, regardless of the radial positions as mentioned in § 4.2. The growth rate of the classical KH instability is defined by the wavelength; perturbations with shorter wavelength grow more rapidly (Drazin & Reid 2004). In cylindrical coordinates, the wavelength is calculated using the corresponding length of the circumference at the radial position as $\lambda_\theta = 2\pi r/k_{\theta,KH}$. That is, for a fixed azimuthal wavenumber, the growth rates of the KH instability accelerate as the radial positions locate increasingly inward in the particular system.

5. Stepwise transitions from non-rotating to rotating RBC

5.1. *Comprehensive explanation for transient behaviours*

Transient behaviours during the spin-up for RBC have been quantified above by PIV analyses of both horizontal and vertical cross-sections. Incorporating all of the discussion, the mechanisms of the transient behaviours may be summarized and detailed as illustrated in figure 17.

In figure 17(*a*), soon after imposing rotation on a fully developed RBC not so far subject to background rotation, the existing thermal turbulent flow structures are disturbed due to the rotation. All presently existing thermally coherent structures such as thermal plumes and large-scale structures disintegrate and all of the fluid is mixed. The whole of the fluid layer responds to the spin-up of any part of the fluid regardless of the initial state. After the first few revolutions of the fluid container, the Ekman boundary layers are formed at the top and bottom walls (Wedemeyer 1964; Greenspan 1968), making the flow structure throughout very similar to a 2-D structure, excluding the boundary layers.

Following this (figure 17*b*), the accelerated region at the sidewall due to the fluid viscosity progressively grows towards the centre of the fluid layer decreasing the size of the core region. The thickness of the accelerated region δ_ν grows with time as $\delta_\nu \propto \sqrt{\nu t}$, and the azimuthal velocity approaches that of the rigid-body rotation velocity $U_\theta = r\Omega$. The Stewartson layers formed at the sidewall enhance the vertical fluid transports that leading onset of convection at the accelerated region, and toroidal convection rolls emerge at the sidewall. Together with the development of the accelerated region, the generation of the convection rolls progresses from the sidewall towards the centre of the fluid layer as illustrated in figure 17(*c*).

The KH instability is induced at the roll boundaries after the emergence of the rolls and azimuthally aligned vortical structures are formed, as illustrated in the top view of figure 17(*c*). A similar mechanism can be seen in the generation of wavy vortex flows in

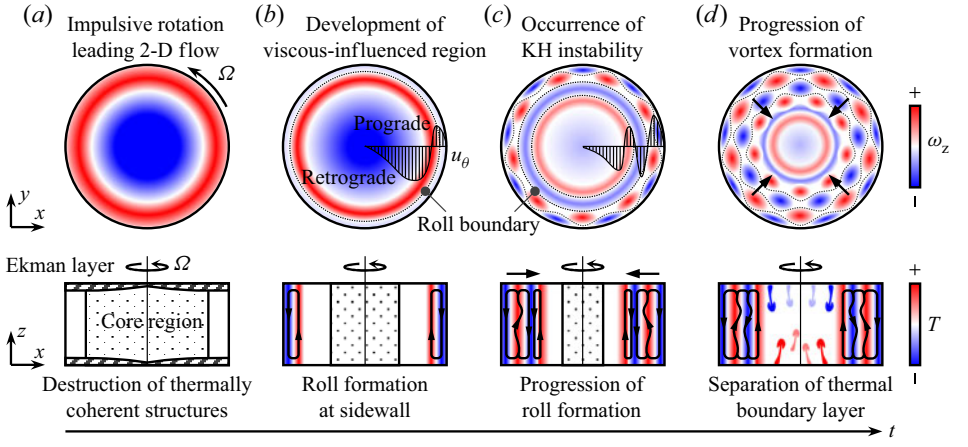

Figure 17. Schematic illustrations of transient behaviours during spin-up of rotating RBC, where time elapse from left to right: (*a*) soon after imposing the rotation; (*b*) roll formation at which the rigid-body rotation achieved; (*c*) vortex formation induced by the KH instability and progression of roll formation towards the centre; (*d*) progression of vortex formation and separation of thermal boundary layer forming columnar vortices in the interior. Each moment is illustrated as top views (top row) and side views (bottom row). Some expressions are exaggerated to enhance understanding.

a Taylor–Couette flow driven by a rotating inner cylinder mentioned elsewhere (Davey, Di Prima & Stuart 1968; Jones 1985; Akonur & Lueptow 2003; Martinand, Serre & Lueptow 2014).

The vortex formations propagate progressively from the sidewall towards the centre of the fluid layer as illustrated in figure 17(*d*). As mentioned in § 4.2, the number of the azimuthally aligned vortices is independent of the radial positions. Accordingly, the azimuthal wavelength of the vortices decreases gradually as they are formed at radially internal regions of the fluid layer. The wall-to-centre progression of the vortex formation is eventually accelerated because fluctuations with smaller wavelengths grow faster than larger ones. When the development of the accelerated region from the sidewall is overtaken by the progression of the vortex formation, any more convection rolls do not emerge. This happens at $r \sim 0.5R$ for all the explored cases as presented in figure 16.

Once large velocity differences between the internal region away from the walls $r < 0.5R$ and the top and bottom boundaries are relaxed because of the progression of the spin-up, the thermal boundary layers at the top and bottom boundaries yield to separation into thermal plumes. These thermal plumes are developed into columnar vortices due to the Coriolis force. Accordingly, after the formation of the convection rolls has terminated, the internal region away from the walls without rolls are dominated by the columnar vortices originating in the thermal plumes. The columnar vortices provide an efficient heat transfer throughout the vortices via the Ekman pumping. The size of the internal columnar vortices is smaller than that of the outer vortices induced by the KH instability as shown in figure 16, resulting in the outer vortices gradually altering their structure to become narrower for optimal heat transfer, as suggested by Sakai (1997).

5.2. *Spin-up time scale unique in rotating RBC*

As summarized in § 5.1, the transient behaviours in the spin-up of RBC emerge in order, and it may be assumed that correspondingly several time scales are embedded in the spin-up process.

The fastest time scale is the system rotation time scale $\tau_\Omega = O(10^{-1}\ \mathrm{s})$ in which the Ekman boundary layers are formed at the top and bottom boundaries (see figure 17*a*). Subsequently the flow approaches the rigid-body rotation in the Ekman spin-up time scale $\tau_E = O(10^{1}\ \mathrm{s})$. The accelerated region at the sidewall develops towards the centre, and the thickness of the region can be estimated as $\delta_v \propto \sqrt{\nu t} \propto t^{1/2}$. As the accelerated region is sufficiently calm for yielding the onset of convection, toroidal convection rolls are formed at the region. In the present study, the growth of the thermal boundary layers is slower than that of the Ekman boundary layers, because the Pr number is larger than unity ($Pr = \nu/\kappa > 1$) with water as the test fluid. Accordingly, the formation of convection rolls propagates radially inwards together with the growth of the accelerated region at the sidewall. Examples for showing more prominent results can be seen in experiments performed by Koschmieder (1968) who used a 100 cSt silicon oil with $Pr = O(10^2)$. In his experiments, the formation of the axisymmetric convection rolls have propagated into the centre of the cylindrical fluid layer with no azimuthal distortion, unlike the present study, as a high viscous fluid allowed fast propagation of the rigid-body rotation. Contrary to this, suppose a low Pr fluid is used as the test fluid, then a well-regulated progression of roll formation may not be observed, and instead oscillatory convection or the occurrence of turbulent convection dominated by thermal plumes could be expected to be initiated from the beginning (Krishnamurti 1973; Clever & Busse 1987).

Vortical structures are generated at the roll boundaries by the KH instability, and the formation of these progresses from the sidewall towards the centre. The wall-to-centre progression of the vortex formation is faster than that of the roll formation because the instability grows faster as it happens at the radially internal positions. In the farther internal region $r < 0.5R$, no convection rolls form because the wall-to-centre progression of the roll formation is overtaken by that of the vortex formation.

Instead of roll formation, thermal plumes forming columnar vortices are generated as there is separation of the thermal boundary layers in the internal region. As the system is initially unstable, the local Ra values within the thermal boundary layers are larger than the Ra_c values. However, large velocity differences between the core region which are not accelerated by the viscosity, and the top and bottom boundary layers, suppress the separation of the thermal boundary layers, and the boundary layers may be supercritical states. Once the velocity differences are sufficiently relaxed together with the development of the accelerated region, the separation of the thermal boundary layers forms thermal plumes. That is, the onset of rotating convection is abruptly realized with time. As if to back up this simple explanation, the columnar vortices suddenly appear in the internal region ($r < 0.5R$) as indicated by the ellipses in figure 11, once after the strong 2-D flow in the core region becomes negligible. In particular, the sudden appearance of the columnar vortices is more visible in the larger Γ case (figure 11*b*). This plume formation in the interior region may be possible to observe when thermal forces are imposed on a rigidly rotating fluid.

Comparing figure 11(*a*,*b*), the whole of the stepwise transitions discussed above are relatively ambiguously appearing in the smaller Γ cylinder. Regarding the aspect ratios of the fluid vessels, $0.656 \leq \Gamma \leq 2.00$, used elsewhere (Boubnov & Golitsyn 1986; Vorobieff & Ecke 1998; Zhong *et al.* 2010), the stepwise transitions might be difficult to observe. That is, the transient behaviours that occur in a stepwise fashion during the spin-up of rotating RBC are established because of the use of the fluid layer with the moderate aspect ratio, $\Gamma = 4.75$ in the present study. Incorporating all the transient

behaviours occurring in order together with the development of the accelerated region from the sidewall, the spin-up time scale unique to rotating RBC should be a few to 10 times longer than the Ekman spin-up time scale τ_E.

6. Concluding remarks

To elucidate details of transient behaviours during spin-up of rotating RBC, systematic laboratory experiments using water as the test fluid were conducted by imposing a rotation on a fully developed thermal convection with Rayleigh numbers $Ra = 2.0 \times 10^6$ and 1.0×10^7. The Taylor number $3.0 \times 10^6 \leq Ta \leq 2.0 \times 10^8$ corresponding to the convective Rossby number $0.0378 \leq Ro \leq 0.690$ was given. Stepwise transitions from an RBC not so far subject to background rotation to a rotating RBC were observed through individually performed visualization experiments in horizontal and vertical cross-sections of two different aspect ratio cylinders. By means of PIV both the horizontal and vertical flow fields were measured and a quantitative understanding was made possible. Soon after imposing the rotation, all thermal plumes or larger coherent structures appearing as a result of thermal convection disintegrated due to the intense viscous dissipation of the rotation. The resulting flow state became identical to that of spin-up from rest without thermal forcing. Together with the growth of the accelerated region due to the fluid viscosity, formation of the convection rolls forming ring or spiral structures propagate from the sidewall towards the centre coinciding with the rotational axis of the fluid layer. Meridional circulations of the convection rolls transport low and high density fluid from the bottom and top boundaries to the interior. As a result, high, but opposite azimuthal momentum is aligned alternately in the radial direction, which develops prograde and retrograde fluid motions in the rotating system. Moreover, alternate radial density distributions are generated due to the existence of the toroidal convection rolls. Accordingly the KH instability evolves gradually in the azimuthal direction with radial amplitude at which the vertical flows, roll boundaries, exist and lead to the formation of azimuthally aligned vortices along the roll boundaries. Wavenumbers equivalent to the number of vortices, are identical for a fixed experimental condition regardless of the radial positions since the wavenumber of the KH instability only depends on Ro. The vortex size decreases with the progression of the instability towards the centre. The minimum size of the vortex induced by the KH instability does not exceed the size of the columnar vortices formed in an equilibrium state of a rotating RBC. Wall-to-centre progression of the roll formation is always caught up around the intermediate radius of the cylinder by that of vortex formation. At radially internal regions of the fluid layer where no vortices are present due to the KH instability, separation of the thermal boundary layers occurs and thermal plumes are emitted to form columnar vortices. Vortices induced by the KH instability alter the horizontal size to become narrower so as to carry optimal heat transfer of an equilibrium state of rotating RBC. Finally, the time scales dominating all the transient behaviours during the spin-up of rotating RBC were found to be explained by the time scales of each stepwise phenomenon.

Supplementary movies. Supplementary movies are available at https://doi.org/10.1017/jfm.2020.1052.

Funding. The authors are grateful for the financial support by a Grant-in-Aid for JSPS Fellows (grant number JP19J20096).

Declaration of interest. The authors report no conflict of interest.

Author ORCIDs.
D. Noto https://orcid.org/0000-0003-3713-4777;
Y. Tasaka https://orcid.org/0000-0002-8943-4803;
T. Yanagisawa https://orcid.org/0000-0001-6289-938X;
T. Miyagoshi https://orcid.org/0000-0002-8908-9990.

References

Akonur, A. & Lueptow, R.M. 2003 Three-dimensional velocity field for wavy Taylor–Couette flow. *Phys. Fluids* **15** (4), 947–960.
Benton, E.R. & Clark, A. Jr. 1974 Spin-up. *Annu. Rev. Fluid Mech.* **6** (1), 257–280.
Boubnov, B.M. & Golitsyn, G.S. 1986 Experimental study of convective structures in rotating fluids. *J. Fluid Mech.* **167**, 503–531.
Cheng, J.S., Aurnou, J.M., Julien, K. & Kunnen, R.P.J. 2018 A heuristic framework for next-generation models of geostrophic convective turbulence. *Geophys. Astrophys. Fluid Dyn.* **112** (4), 277–300.
Clever, R.M. & Busse, F.H. 1987 Nonlinear oscillatory convection. *J. Fluid Mech.* **176**, 403–417.
Davey, A., Di Prima, R.C. & Stuart, J.T. 1968 On the instability of Taylor vortices. *J. Fluid Mech.* **31** (1), 17–52.
Drazin, P.G. & Reid, W.H. 2004 *Hydrodynamic Stability*. Cambridge University Press.
Fujita, K., Tasaka, Y., Yanagisawa, T., Noto, D. & Murai, Y. 2020 Three-dimensional visualization of columnar vortices in rotating Rayleigh–Bénard convection. *J. Vis.* **23** (4), 635–647.
Grannan, A.M., Favier, B., Le Bars, M. & Aurnou, J.M. 2016 Tidally forced turbulence in planetary interiors. *Geophys. J. Intl* **208** (3), 1690–1703.
Gray, D.D. & Giorgini, A. 1976 The validity of the Boussinesq approximation for liquids and gases. *Intl J. Heat Mass Transfer* **19** (5), 545–551.
Greenspan, H.P. 1968 *The Theory of Rotating Fluids*. Cambridge University Press.
Greenspan, H.P. & Howard, L.N. 1963 On a time-dependent motion of a rotating fluid. *J. Fluid Mech.* **17** (3), 385–404.
Horn, S. & Shishkina, O. 2014 Rotating non-Oberbeck–Boussinesq Rayleigh–Bénard convection in water. *Phys. Fluids* **26** (5), 055111.
Jones, C.A. 1985 The transition to wavy Taylor vortices. *J. Fluid Mech.* **157**, 135–162.
Jones, C.A. 2011 Planetary magnetic fields and fluid dynamos. *Annu. Rev. Fluid Mech.* **43**, 583–614.
Julien, K., Rubio, A.M., Grooms, I. & Knobloch, E. 2012 Statistical and physical balances in low Rossby number Rayleigh–Bénard convection. *Geophys. Astrophys. Fluid Dyn.* **106**, 392–428.
King, E.M., Stellmach, S. & Aurnou, J.M. 2012 Heat transfer by rapidly rotating Rayleigh–Bénard convection. *J. Fluid Mech.* **691**, 568–582.
Koschmieder, E.L. 1968 Convection on a non-uniformly heated, rotating plane. *J. Fluid Mech.* **33** (3), 515–527.
Krishnamurti, R. 1973 Some further studies on the transition to turbulent convection. *J. Fluid Mech.* **60** (2), 285–303.
Liu, Y. & Ecke, R.E. 2009 Heat transport measurements in turbulent rotating Rayleigh–Bénard convection. *Phys. Rev.* E **80**, 036314.
Martinand, D., Serre, E. & Lueptow, R.M. 2014 Mechanisms for the transition to waviness for Taylor vortices. *Phys. Fluids* **26** (9), 094102.
Noto, D., Tasaka, Y., Yanagisawa, T. & Murai, Y. 2019 Horizontal diffusive motion of columnar vortices in rotating Rayleigh–Bénard convection. *J. Fluid Mech.* **871**, 401–426.
Noto, D., Tasaka, Y., Yanagisawa, T., Park, H.J. & Murai, Y. 2018 Vortex tracking on visualized temperature fields in a rotating Rayleigh–Bénard convection. *J. Vis.* **21** (6), 987–998.
Ravichandran, S. & Wettlaufer, J.S. 2020 Transient convective spin-up dynamics. *J. Fluid Mech.* **897**, A24.
Sakai, S. 1997 The horizontal scale of rotating convection in the geostrophic regime. *J. Fluid Mech.* **333**, 85–95.
Stevens, R.J.A.M., Clercx, H.J.H. & Lohse, D. 2013 Heat transport and flow structure in rotating Rayleigh-Bénard convection. *Eur. J. Mech. (*B*/Fluids)* **40**, 41–49.
Vorobieff, P. & Ecke, R.E. 1998 Transient states during spin-up of a Rayleigh–Bénard cell. *Phys. Fluids* **10** (10), 2525–2538.
Wedemeyer, E.H. 1964 The unsteady flow within a spinning cylinder. *J. Fluid Mech.* **20** (3), 383–399.

WEIDMAN, P.D. 1976 On the spin-up and spin-down of a rotating fluid. Part 1. Extending the Wedemeyer model. *J. Fluid Mech.* **77** (4), 685–708.

WEISS, S. & AHLERS, G. 2011 Heat transport by turbulent rotating Rayleigh–Bénard convection and its dependence on the aspect ratio. *J. Fluid Mech.* **309**, 1–20.

ZHONG, J.-Q., PATTERSON, M.D. & WETTLAUFER, J.S. 2010 Streaks to rings to vortex grids: generic patterns in transient convective spin up of an evaporating fluid. *Phys. Rev. Lett.* **105** (4), 044504.